NANO LETTERS Letter
Cite This: Nano Lett. 2018, 18, 26−31 pubs.acs.org/NanoLett

Anomalous Temperature Dependence in Metal−Black Phosphorus Contact

Xuefei Li,[†] Roberto Grassi,[‡] Sichao Li,[†] Tiaoyang Li,[†] Xiong Xiong,[†] Tony Low,[*,‡] and Yanqing Wu[*,†]

[†]Wuhan National High Magnetic Field Center and School of Electrical and Electronic Engineering, Huazhong University of Science and Technology, Wuhan 430074, China

[‡]Department of Electrical and Computer Engineering, University of Minnesota, Minneapolis, Minnesota 55455, United States

Supporting Information

ABSTRACT: Metal−semiconductor contact has been the performance limiting problem for electronic devices and also dictates the scaling potential for future generation devices based on novel channel materials. Two-dimensional semiconductors beyond graphene, particularly few layer black phosphorus, have attracted much attention due to their exceptional electronic properties such as anisotropy and high mobility. However, due to its ultrathin body nature, few layer black phosphorus−metal contact behaves differently than conventional Schottky barrier (SB) junctions, and the mechanisms of its carrier transport across such a barrier remain elusive. In this work, we examine the transport characteristic of metal−black phosphorus contact under varying temperature. We elucidated the origin of apparent negative SB heights extracted from classical thermionic emission model and also the phenomenon of metal−insulator transition observed in the current−temperature transistor characteristic. In essence, we found that the SB height can be modulated by the back-gate voltage, which beyond a certain critical point becomes so low that the injected carrier can no longer be described by the conventional thermionic emission theory. The transition from transport dominated by a Maxwell−Boltzmann distribution for the high energy tail states, to that of a Fermi distribution by low energy Fermi sea electrons, is the physical origin of the observed metal−insulator transition. We identified two distinctive tunneling limited transport regimes in the contact: vertical and longitudinal tunneling.

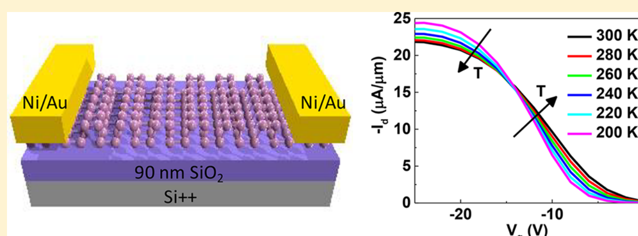

KEYWORDS: *Black phosphorus, Schottky barrier, metallic−insulator transition, contact resistance*

Two-dimensional (2D) layered materials have attracted much attention because of their unique properties for next generation electrical and optoelectronic device applications.[1−6] While graphene has excellent mobility and broadband absorption, its gapless nature is a major obstacle for logic transistor applications.[7] However, the transition metal dichalcogenides (TMDCs) represent another set of 2D layered materials, which exhibit tunable bandgap in the range of 0.4−2.3 eV and modest carrier mobility.[8−10] Well-behaved n-type field-effect transistors (FETs) with high on/off ratio, logic circuits, and amplifiers with high gain, as well as sensors, have been demonstrated using MoS_2.[11−14] Given the unique ultrathin body nature, 2D semiconductors are relatively insensitive to short channel effects, which is highly desirable for low-power nanoscale transistors. Very recently, a new layered 2D semiconductor material, black phosphorus (BP), with a direct bandgap of ~0.3 eV in bulk to 2.0 eV in a single layer has been explored. It was found that few-layer BP transistors can exhibit an on/off ratio of 10^5 and mobility up to 1000 $cm^2/V{\cdot}s$ at room temperature.[15−19] Radio Frequency and excellent photodetectors properties have been reported.[20,21] Also, the first 2D CMOS inverter consisting of phosphorene pMOS and MoS_2 nMOS transistors has been demonstrated, allowing for the prospect of 2D semiconductors in future electronic applications.[17]

Despite the recent progress, contact resistance (R_c) between 2D materials and metal limits the performance of these devices and poses a severe challenge for the applications in electronics and optoelectronics. There is also a lack of understanding of the carrier transport mechanisms through these contacts, albeit this problem is beginning to receive more attention.[22] The electrical characteristics of BP transistors have been shown to be dominated by the Schottky barriers (SB), which are modulated by back-gate voltage.[23] To date, the basic physics mechanism of electrical contact between the BP channel and metal remains unclear. Avsar et al. reported a negative SB height ranging from −17 to −2.5 meV for BP/graphene/boron nitride using the thermionic emission model, suggesting that the transport is in a regime where the model breaks down. A new theoretical model is necessary to explain this phenomenon in a 2D system.[24] Meanwhile, the physical mechanism responsible for the metallic−insulator crossover observed for the transfer characteristics of 2D devices remains in dispute.[24−33] In this work, we

Received: May 30, 2017
Revised: December 5, 2017
Published: December 5, 2017

 © 2017 American Chemical Society
DOI: 10.1021/acs.nanolett.7b02278
Nano Lett. 2018, 18, 26−31

seek to address the issues mentioned above experimentally, in conjunction with a new theoretical model.

Results. *Device Fabrication and Transport Measurement.* The devices consist of few-layer BP flakes with thickness from 5.3 to 13.4 nm, deposited onto a Si/SiO_2 (90 nm) substrate by mechanical exfoliation. Figure 1a shows the schematic view of

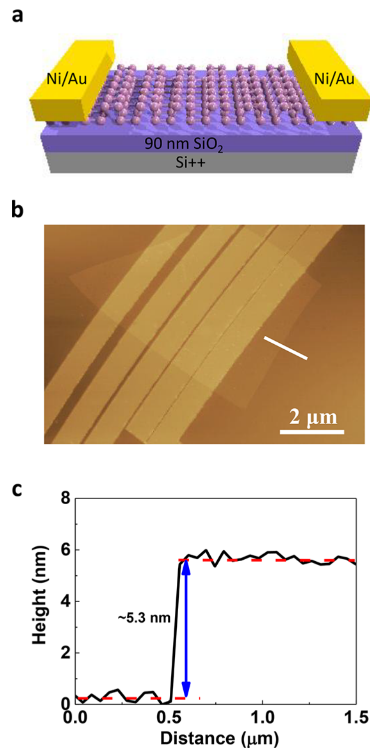

Figure 1. Device structures and the thickness of black phosphorus. (a) Schematic and (b) AFM image of the few-layer BP devices. The scale bar is 2 μm. (c) BP flake with a measured thickness of ∼5.3 nm by AFM. The contact bars with length of 0.7 μm was defined by e-beam lithography.

the back-gated field-effect transistor configuration used in here. Figure 1b shows an atomic force microscopy image of few-layer BP back-gated transistors, showing the BP devices designed for measurements with different channel lengths. Ni/Au (30/50 nm) was deposited via e-beam evaporation for metal contacts. The thickness of the BP flake is around 5.3 nm measured by the AFM, as shown in Figure 1c. The Raman spectrum in Figure S1 confirms the properties of BP flake.

Figure 2a,b shows the transfer curves of few-layer BP FET with a 200 nm channel length at 300 and 20 K, respectively. The negative shift of transfer curves at 20 K is mainly attributed to the frozen charge traps from the SiO_2 film and the SiO_2−BP interface.[34] In addition, the off-currents are found to be very low at 20 K. The off current (I_{off}) is mainly dominated by the thermionic emission of carriers through the metal−BP Schottky barrier, which is proportional to $\exp(-e\Phi_b/kT)$, where e is the electron charge, Φ_b is the Schottky barrier height, k is the Boltzmann constant, and T is the temperature. When temperature decreases, I_{off} decreases accordingly, which is consistent with previous results.[35,36] Figure 2c,d shows the output characteristics of the same device with a drain voltage from 0 to −2 V and a back-gate sweep from 40 to −30 V at 300 and 20 K, respectively. The on-state current is 300 μA/μm with gate voltage V_g = −30 V and drain voltage V_d = −2 V, and it

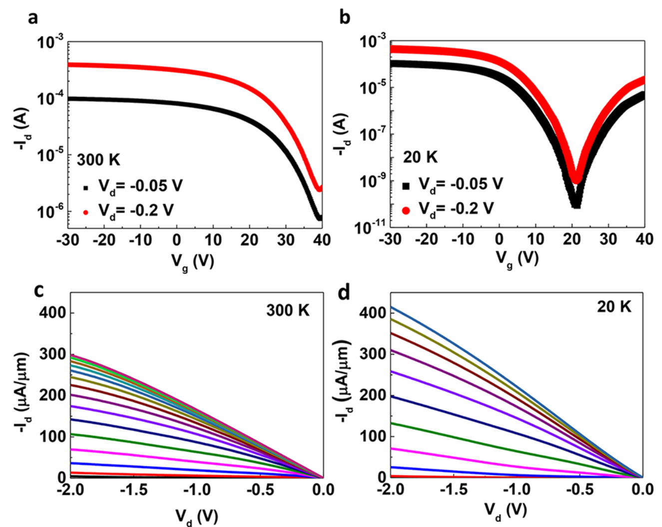

Figure 2. Electrical characterization of black phosphorus FETs at 300 and 20 K. Transfer characteristics of the 0.2 μm BP transistor with V_d = −0.05 and −0.2 V at (a) 300 and (b) 20 K. The thickness is ∼13.4 nm. Output characteristics of the same device at (c) 300 and (d) 20 K. At 300 K, V_g is from 40 to −30 V with steps of −5 V. At 20 K, V_g is from 20 to −30 V with steps of −5 V.

increases further up to 416 μA/μm at 20 K due to the increase of mobility at low temperatures.[15,16,34]

It is well-known that contact resistance has a strong dependence on the back-gate bias (V_g) in 2D materials system.[12,23] To investigate the effect of V_g on the performance of BP transistors, I_d−V_d characteristics of a 5.3 nm-thick device with fixed $V_g - V_{min}$ = −35 and −15 V from 300 to 20 K are shown in Figure 3a (the gate voltage of the minimum current is denoted here as V_{min}). At $V_g - V_{min}$ = −35 V, I_d increases from 30 to 41 μA/μm with decreasing temperatures down to 20 K, whereas I_d keeps decreasing with decreasing temperature at V_g

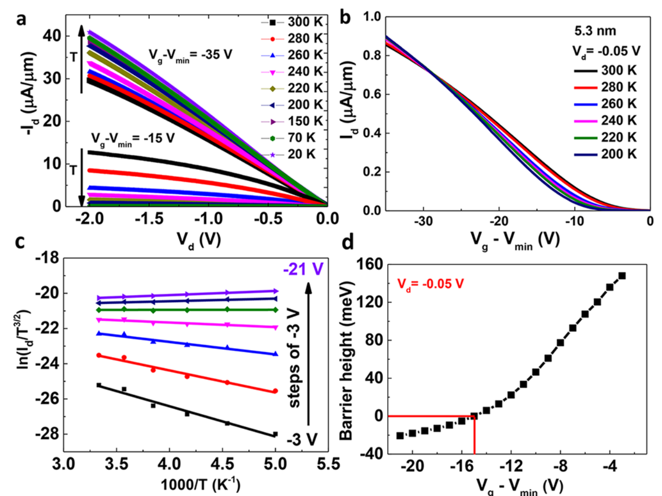

Figure 3. Temperature-dependent transport of black phosphorus FETs. (a) Output characteristics of the BP device at two different gate voltages with temperature ranging from 300 to 20 K. The BP thickness is ∼5.3 nm. (b) Transfer characteristics of the same device at various temperatures (300 to 200 K with a 20 K step). V_d is −50 mV. (c) Arrhenius plots of the BP device at various gate voltages for calculations of the Schottky barrier heights. (d) Extracted Schottky barrier heights as a function of $V_g - V_{min}$.

DOI: 10.1021/acs.nanolett.7b02278
Nano Lett. 2018, 18, 26−31

− V_{min} = −15 V. The observed opposite transport behavior implies different transport mechanisms under different back-gate voltage. To obtain a better comparison of the transfer characteristics at different temperatures, we plotted I_d as a function of $V_g - V_{min}$ from 300 to 200 K as shown in Figure 3b. It is clear that there is a crossover in the transfer curves at around $V_g - V_{min} = -28.6$ V. Drain current increases with decreasing temperature when $V_g - V_{min} < -28.6$ V. However, I_d decreases with decreasing temperature when $V_g - V_{min}$ is larger than −28.6 V. The same phenomena are common among other devices as shown in Figure S3 with different channel thickness. This is consistent with previous studies using graphene electrodes to 2D semiconductors and is commonly attributed to the presence of a metal−insulator transition (MIT) of the channel material.[24,25,27−31] Here, we develop a new model to explain this phenomenon in terms of contact-limited effects instead, as discussed later. In order to study the Schottky barrier height, we fit the data at $V_d = -0.05$ V to the classical thermionic emission equation of Schottky barriers:[26,37]

$$I_d = AA^*T^{3/2}\exp\left[-\frac{e}{K_BT}\left(\phi_b - \frac{V_{ds}}{n}\right)\right] \quad (1)$$

where A is the contact area, A^* is the Richardson constant, e is the electron charge, k_B the Boltzmann constant, and n is the ideality factor. Figure 3c shows the Arrhenius plot of $\ln(I_d/T^{3/2})$ versus $1000/T$ for various values of $V_g - V_{min}$ from −3 to −21 V. We can see that the slope of $\ln(I_d/T^{3/2})$ vs $1000/T$ changes from negative to positive with decreasing V_g, and the extracted Schottky barrier height is shown in Figure 3d. Similar to the graphene−BP contact,[24] the Schottky barrier height of nickel−BP contact decreases from 148 to 0 meV with the back-gate voltage changing from −3 to −15 V. For $V_g - V_{min} > -15$ V, the thermionic emission dominates the transport, resulting in the drain current reduction with decreasing temperatures. However, for $V_g - V_{min} < -15$ V, negative Schottky barrier heights were extracted using the above classical thermionic emission model, indicating the model itself is no longer valid in this bias region. This behavior has been observed recently in other 2D systems, and phenomenological explanations were adopted.[24−26,31] It is commonly attributed to the onset of the tunneling effect; however, thorough theoretical explanations are still lacking, especially in this ultrathin material system where the Fermi level of the semiconductor underneath the contact metal can also be tuned by the back-gate voltage, which in turn gives a different origin for this phenomenon as discussed in details below.

Quantum Transport Calculation. The BP device is simulated using a self-consistent ballistic quantum transport solver based on the nonequilibrium Green's function formalism.[38] The device structure is similar to the experimental one (top contact, back-gate, and 90 nm thick SiO_2 dielectric) and the BP thickness is fixed at 5 nm. Since the device is symmetric with respect to source and drain, and only low-bias transport is considered, only half of the transistor structure, consisting of the source metal/BP contact plus half of the transistor channel, is actually simulated as shown in Figure 4a. The length of the contact is 50 nm. The drain voltage V_d is applied between the right end of the channel and the source contact and is fixed at −0.01 V in all simulations. The metal work function is chosen such that the metal Fermi level is close to the BP valence band edge, which favors hole conduction, per the case in the experiment. Details of the simulation model, including the

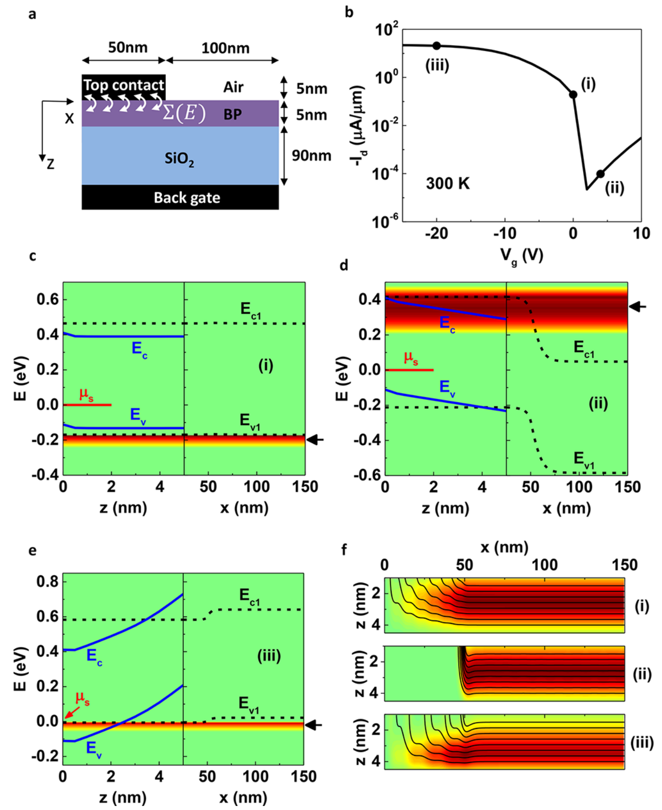

Figure 4. Transport regimes of simulated metal/black phosphorus junction. (a) Schematic of the simulated BP device. (b) Transfer characteristics at 300 K and $V_d = -0.01$ V. (c−e) Vertical (left panel) and longitudinal (right panel) band profiles at $V_g = 0$ V (c), $V_g = 4$ V (d), and $V_g = -20$ V (e). A color plot of the energy-resolved current spectrum $I_d(E)$ is also shown: dark red (light green) corresponds to high (low) current value. Each plot has a different color scale. (f) Spatially resolved current density vector at V_g = 0, 4, and −20 V and at the energies indicated by arrows in panels (c), (d), and (e), respectively. The lines indicate the current direction, while the color scale is proportional to the current magnitude.

treatment of the metal/BP interface, are provided in the Supporting Information.

Figure 4b shows the simulated $I_d - V_g$ characteristic at room temperature. It shares similarities with the experimental curves in Figure 2a,b. In particular, a hole branch for $V_g < 2$ V and an electron branch for $V_g > 2$ V can be identified. In turn, the hole branch can be decomposed into two different regions separated by a transition point, which corresponds to the flat-band voltage $V_g = 0$ V. The different regimes can be understood with the help of the subband profiles shown in the right panels of Figure 4c−e for three different gate voltages, as labeled in Figure 4b. Here, E_{c1} and E_{v1} denote the first conduction and valence subband edges, respectively. Note that the SB height is defined as the difference between the subband edge E_{c1} or E_{v1} in the contact region ($x < 50$ nm) and the source Fermi level μ_s = 0 eV. In the flat-band condition $V_g = 0$ (Figure 4c), transport [see the superimposed color plot of the energy-resolved current spectrum $I_d(E)$] is due to thermionic emission of holes above the SB.

For larger gate voltage, the valence band edge in the channel is lower than at the interface with the contact; hence, holes traversing the channel see a larger barrier than the SB height. The lowering of the valence band in the channel with increasing V_g explains why the current decreases exponentially.[39] At the

DOI: 10.1021/acs.nanolett.7b02278
Nano Lett. 2018, 18, 26−31

bias point V_g = 4 V (Figure 4d), the hole thermionic current gets indeed suppressed, while the dominant contribution is given by electron tunneling below the SB defined by the value of E_{c1} in the contact region. It should be noted, however, that since the geometry is two-dimensional one should consider the 2D potential profile to get a complete physical picture. A vertical cutline of the 2D potential for electrons and holes, i.e. bulk band edges E_c and E_v, in the middle of the contact region (x = 25 nm) is shown in the left panel of each of Figures 4c–e (full plots as a function of both x and z are shown in the Supporting Information). As a result of the vertical band bending, holes are pushed toward the interface with the back oxide,[40] and the SB height for holes is lowered for increasing negative V_g (Figure 4e). Consequently, the hole branch of the characteristics is always dominated by above-the-barrier transport. Note that, strictly speaking, transport at V_g = −20 V should be considered as a tunneling process, too, since the carriers moving from the metal to the semiconductor have to cross a tunneling barrier in the vertical direction. This regime could be named "vertical tunneling" rather than thermionic. However, due to the small thickness of the vertical tunneling barrier (≈2 nm), the transport mechanism is actually very similar to the pure thermionic case. The 2D representation of the current flow in Figure 4f reveals that electron tunneling occurs mostly at the contact edge and thus resembles a 1D tunneling process ("longitudinal tunneling"). However, in the pure thermionic and vertical tunneling cases, the entire length of the contact contributes to the current flow.

We study next the temperature dependence, focusing on the hole branch at V_g < 0 V. Figure 5a shows the simulated $I_d - V_g$ characteristics in linear scale and for temperatures ranging from 300 to 200 K. A striking similarity between the numerical and experimental results is the presence of a crossover in the transfer characteristics. For the simulated device, the crossover occurs around V_g = −15 V: the drain current increases with decreasing temperature when V_g < −15 V and decreases when V_g > −15 V. We rely on the Landauer formalism,[38] which expresses the drain current as an integral over energy E of the quantity

$$I_d(E) = -\frac{2e}{h}T(E)(F_s - F_d) \tag{2}$$

where $T(E)$ is the transmission function and the supply function $F_{s/d}$ is defined as

$$F_{s/d} = \sqrt{\frac{m_y k_B T}{2\pi\hbar^2}}\mathcal{F}_{-1/2}\left(\frac{E - \mu_{s/d}}{k_B T}\right) \tag{3}$$

with h the Plank constant, $\hbar = h/(2\pi)$, m_y the hole transverse effective mass, $\mathcal{F}_{-1/2}$ the Fermi integral of order −1/2, and μ_d the drain Fermi level.

The transmission function is plotted versus energy at room temperature and at two different gate biases, V_g = −10 and −20 V, in Figure 5b. When the gate voltage is decreased, the subband edge E_{v1} shifts to higher energies and so does the transmission function. It should be noted that, different from a pure thermionic regime, the transmission function decays as a function of energy above the SB. Indeed, treating transport as a vertical tunneling process, it is possible to show that $T(E) \propto (E_{v1} - E)^{-1/2}$, where the proportionality constant is related to the tunneling rate from the metal to the semiconductor.[41] The shape of $F_s - F_d$ as a function of energy and temperature is also superimposed in Figure 5b. The plot reveals a crossover that

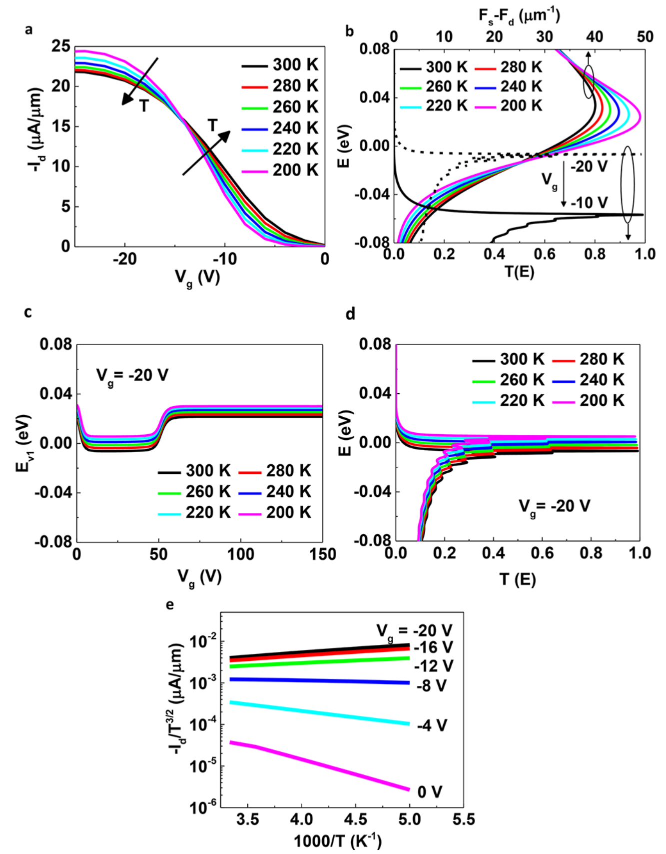

Figure 5. Temperature-dependent transport of simulated metal–black phosphorus junction. (a) Transfer characteristics of the simulated device at various temperatures and V_d = −0.01 V. (b) Difference of source and drain supply functions versus energy at various temperatures. Superimposed are the spectra of the transmission function at V_g = −10 V (solid line) and V_g = −20 V (dashed line) at 300 K. (c) Longitudinal profile of the first valence subband edge at various temperatures and V_g = −20 V. (d) Transmission function versus energy at various temperatures and V_g = −20 V. (e) Arrhenius plot of drain current at various gate voltages.

resembles the one in the transfer characteristics, located around −0.01 eV: the function increases with decreasing temperature for E > −0.01 eV and decreases for E < −0.01 eV. As the transmission function shifts to higher energy with decreasing V_g, more contribution to the integral of eq 2 comes from the energy range where $\partial(F_s - F_d)/\partial T < 0$ and eventually leads to $\partial|I_d|/\partial T < 0$. Another effect that also contributes to the increase of the drain current with decreasing temperature is a temperature dependence of the energy band diagram (Figure 5c), which results in the transmission function to shift to higher energies when temperature is decreased (Figure 5d). This can be explained with the help of a simple electrostatic model as shown in the Supporting Information. The Arrhenius plot of $\ln(I_d/T^{3/2})$ versus $1000/T$ for various V_g values is shown in Figure 5e. The slope changes from negative to positive when V_g is decreased below −8 V, which is again very similar to the experimental results in Figure 3c. The positive slope is mainly due to the increase of I_d with decreasing temperature for V_g < −15 V. Hence, the insulator to metallic-type temperature dependence can be attributed to the transition from transport dominated by the high energy Fermi tail states to that due to low energy Fermi sea states. In the former, carrier statistics can

DOI: 10.1021/acs.nanolett.7b02278
Nano Lett. 2018, 18, 26−31

be described by a Maxwell–Boltzmann distribution, while the latter only by the Fermi–Dirac distribution.

In summary, the temperature-dependent transport through the metal–BP contact has been investigated through a combination of experimental data and 2D quantum transport simulations. In particular, we have addressed two phenomena, negative SB height and crossover of the transfer characteristics, whose origin has not been completely elucidated so far. We propose that the two effects can be explained on the basis of a contact limited transport model by taking into account the electrostatic modulation of the SB by the back-gate voltage. At sufficiently high negative V_g, the SB height becomes so low that the injected carrier cannot be described anymore by Boltzmann's statistics, leading to the failure of the usual thermionic emission theory and the fact that the current can actually increase with decreasing temperature. Contrary to the common belief, the observed metallic–insulator transition in the contact is not due to the interplay between tunneling and thermionic transport, but rather that of the different carrier statistics of Fermi tail/sea electronic states.

Methods. Few layer BP flakes were mechanically exfoliated from the purchased natural bulk black phosphorus (Smart-elements) onto a 90 nm SiO_2/p++ Si wafer, which was prepatterned with alignment marks. To prevent BP from oxidation, exfoliation was performed in an argon-filled glovebox with oxygen and water concentrations well below 0.1 part-per-million (ppm) to ensure high-quality samples. Prior to device fabrication, the BP films were soaked in acetone and isopropanol to remove tape residues. These were subsequently coated with poly(methyl methacrylate) (PMMA) resist for the next e-beam lithography right after the exfoliation to avoid any possible degradation upon long exposure to air. E-beam lithography was used to define the source/drain region using a Vistec EBPG 5000pES. Ni (30 nm)/Au (50 nm) were deposited using e-beam evaporation under 10^{-6} Pa pressure and lifted off to form the metal contact. No annealing and PMMA passivation were performed after the deposition of the metal contacts. The electrical characterization was carried out in a lakeshore cryogenic probe station under $<10^{-5}$ Torr using an Agilent B1500A parameter analyzer.

■ ASSOCIATED CONTENT

Supporting Information

The Supporting Information is available free of charge on the ACS Publications website at DOI: 10.1021/acs.nanolett.7b02278.

Raman and XPS characterization, temperature dependencies, AFM, and simulation model (PDF)

■ AUTHOR INFORMATION

Corresponding Authors

*E-mail: yqwu@mail.hust.edu.cn.
*E-mail: tlow@umn.edu.

ORCID

Tony Low: 0000-0002-5759-5899
Yanqing Wu: 0000-0003-2578-5214

Author Contributions

X.L. and R.G. contributed equally. Y.W. and T.L. conceived and designed the measurements. X. L., S.L., and T.L. performed all device fabrication and electrical experiments. X.X. performed AFM measurements. R.G. carried out theoretical analysis and calculations. All the authors discussed the results and commented on the manuscript.

Notes

The authors declare no competing financial interest.

■ ACKNOWLEDGMENTS

This project was supported by the Natural Science Foundation of China (Grant Nos. 11404118, 61574066, and 61390504).

■ REFERENCES

(1) Geim, A. K.; Novoselov, K. S. *Nat. Mater.* **2007**, *6*, 183–191.
(2) Radisavljevic, B.; Radenovic, A.; Brivio, J.; Giacometti, V.; Kis, A. *Nat. Nanotechnol.* **2011**, *6*, 147–150.
(3) Wang, Q. H.; Kalantar-Zadeh, K.; Kis, A.; Coleman, J. N.; Strano, M. S. *Nat. Nanotechnol.* **2012**, *7*, 699–712.
(4) Geim, A.; Grigorieva, I. *Nature* **2013**, *499*, 419–425.
(5) Fiori, G.; Bonaccorso, F.; Iannaccone, G.; Palacios, T.; Neumaier, D.; Seabaugh, A.; Banerjee, S. K.; Colombo, L. *Nat. Nanotechnol.* **2014**, *9*, 768–779.
(6) Xia, F.; Wang, H.; Xiao, D.; Dubey, M.; Ramasubramaniam, A. *Nat. Photonics* **2014**, *8*, 899–907.
(7) Schwierz, F. *Nat. Nanotechnol.* **2010**, *5*, 487–496.
(8) Koski, K. J.; Cui, Y. *ACS Nano* **2013**, *7*, 3739–3743.
(9) Miró, P.; Audiffred, M.; Heine, T. *Chem. Soc. Rev.* **2014**, *43*, 6537–6554.
(10) Yazyev, O. V.; Kis, A. *Mater. Today* **2015**, *18*, 20–30.
(11) Li, X. F.; Yang, L. M.; Si, M. W.; Li, S. C.; Huang, M. Q.; Ye, P. D.; Wu, Y. Q. *Adv. Mater.* **2015**, *27*, 1547–1552.
(12) Liu, H.; Neal, A. T.; Ye, P. D. *ACS Nano* **2012**, *6*, 8563–8569.
(13) Wang, H.; Yu, L.; Lee, Y. H.; Shi, Y.; Hsu, A.; Chin, M. L.; Li, L.; Dubey, M.; Kong, J.; Palacios, T. *Nano Lett.* **2012**, *12*, 4674–4680.
(14) Late, D. J.; Huang, Y. K.; Liu, B.; Acharya, J.; Shirodkar, S. N.; Luo, J.; Yan, A.; Charles, D.; Waghmare, U. V.; Dravid, V. P.; Rao, C. N. R. *ACS Nano* **2013**, *7*, 4879–4891.
(15) Li, L.; Yu, Y.; Ye, G.; Ge, Q.; Ou, X.; Wu, H.; Feng, D.; Chen, X.; Zhang, Y. *Nat. Nanotechnol.* **2014**, *9*, 372–377.
(16) Xia, F.; Wang, H.; Jia, Y. *Nat. Commun.* **2014**, *5*, 4458.
(17) Liu, H.; Neal, A. T.; Zhu, Z.; Luo, Z.; Xu, X.; Tománek, D.; Ye, P. D. *ACS Nano* **2014**, *8*, 4033–4041.
(18) Liu, H.; Du, Y.; Deng, Y.; Ye, P. D. *Chem. Soc. Rev.* **2015**, *44*, 2732–2743.
(19) Ling, X.; Wang, H.; Huang, S.; Xia, F.; Dresselhaus, M. S. *Proc. Natl. Acad. Sci. U. S. A.* **2015**, *112*, 4523–4530.
(20) Wang, H.; Wang, X.; Xia, F.; Wang, L.; Jiang, H.; Xia, Q.; Chin, M. L.; Dubey, M.; Han, S. *Nano Lett.* **2014**, *14*, 6424–6429.
(21) Buscema, M.; Groenendijk, D. J.; Blanter, S. I.; Steele, G. A.; van der Zant, S. J.; Castellanos-Gomez, A. *Nano Lett.* **2014**, *14*, 3347–3352.
(22) Allain, A.; Kang, J.; Banerjee, K.; Kis, A. *Nat. Mater.* **2015**, *14*, 1195.
(23) Du, Y.; Liu, H.; Deng, Y.; Ye, P. D. *ACS Nano* **2014**, *8*, 10035–10042.
(24) Avsar, A.; Veramarun, I. J.; Tan, J. Y.; Watanabe, K.; Taniguchi, T.; Castro Neto, A. H.; Özyilmaz, B. *ACS Nano* **2015**, *9*, 4138–4145.
(25) Cui, X.; Lee, G. H.; Kim, Y. D.; Arefe, G.; Huang, P. Y.; Lee, C. H.; Chenet, D. A.; Zhang, X.; Wang, L.; Ye, F.; Pizzocchero, F.; Jessen, B. S.; Watanabe, K.; Taniguchi, T.; Muller, D. A.; Low, T.; Kim, P.; Hone, J. *Nat. Nanotechnol.* **2015**, *10*, 534–540.
(26) Yu, L.; Lee, Y. H.; Ling, X.; Santos, E. J. G.; Shin, Y. C.; Lin, Y.; Dubey, M.; Kaxiras, E.; Kong, J.; Wang, H.; Palacios, T. *Nano Lett.* **2014**, *14*, 3055–3063.
(27) Baugher, B. W.; Churchill, H. O.; Yang, Y.; Jarillo-Herrero, P. *Nano Lett.* **2013**, *13*, 4212–4216.
(28) Radisavljevic, B.; Kis, A. *Nat. Mater.* **2013**, *12*, 815–820.
(29) Schmidt, H.; Wang, S.; Chu, L.; Toh, M.; Kumar, R.; Zhao, W.; Castro Neto, A. H.; Martin, J.; Adam, S.; Özyilmaz, B. *Nano Lett.* **2014**, *14*, 1909–1913.

(30) Yu, Z.; Pan, Y.; Shen, Y.; Wang, Z.; Ong, Z. Y.; Xu, T.; Xin, R.; Pan, L.; Wang, B.; Sun, L.; Wang, J.; Zhang, G.; Zhang, W. Y. *Nat. Commun.* **2014**, *5*, 5290.
(31) Liu, Y.; Cheng, H.; Yang, S.; Zhu, E.; He, Q.; Ding, M.; Li, D.; Guo, J.; Weiss, N. O.; Huang, Yu.; Duan, X.; Wu, H. *Nano Lett.* **2015**, *15*, 3030−3034.
(32) Saito, Y.; Iwasa, Y. *ACS Nano* **2015**, *9*, 3192−3198.
(33) Solomon, P. *IEEE Electron Device Lett.* **2010**, *31*, 618.
(34) Li, T.; Zhang, Z.; Li, X.; Huang, M.; Li, S.; Li, S.; Wu, Y. *Appl. Phys. Lett.* **2017**, *110*, 163507.
(35) Xia, F.; Farmer, D.; Lin, Y.; Avouris, P. *Nano Lett.* **2010**, *10*, 715−718.
(36) Kamalakar, M.; Madhushankar, B. N.; Dankert, A.; Dash, S. *Small* **2015**, *11*, 2209−2216.
(37) Chen, J. R.; Odenthal, P. M.; Swartz, A. G.; Floyd, G. C.; Wen, H.; Luo, K. Y.; Kawakami, R. K. *Nano Lett.* **2013**, *13*, 3106−3110.
(38) Datta, S. *Electronic Transport in Mesoscopic Systems*; Cambridge University Press, 1995.
(39) Penumatcha, A. V.; Salazar, R. B.; Appenzeller, J. *Nat. Commun.* **2015**, *6*, 8948.
(40) Saito, Y.; Nakamura, Y.; Bahramy, M. S.; Kohama, Y.; Ye, J.; Kasahara, Y.; Nakagawa, Y.; Onga, M.; Tokunaga, M.; Nojima, T.; Yanase, Y.; Iwasa, Y. *Nat. Phys.* **2015**, *12*, 144−149.
(41) Grassi, R.; Wu, Y.; Koester, S. J.; Low, T. *Phys. Rev. B: Condens. Matter Mater. Phys.* **2017**, *96*, 165439.

DOI: 10.1021/acs.nanolett.7b02278
Nano Lett. 2018, 18, 26−31